



Evolution of Microstructure and Mechanical Properties of Graphitized Fe–0.55C–2.3Si Steel During Quenching and Tempering Treatment

Ye Jin Kim¹ · Sang Woo Bae¹ · Nam Suk Lim² · Sung Hyuk Park¹

Received: 16 March 2020 / Accepted: 22 April 2020 / Published online: 16 May 2020
© The Korean Institute of Metals and Materials 2020

Abstract

This study investigates the variations in the microstructure and mechanical properties of a medium-carbon high-Si steel (Fe–0.55C–2.3Si) during graphitization heat treatment and subsequent quenching and tempering heat treatment. The microstructure comprising ferrite and pearlite of the as-rolled sample changes to a more ductile microstructure with fine graphites uniformly dispersed in the ferrite matrix after graphitization treatment. These formed graphites are completely dissolved into the ferrite matrix after austenitizing treatment at 900 °C, but preexisting graphite positions remains as voids. The average size and number density of voids are nearly identical to those of the pre-existed graphites. The subsequent tempering treatments at 300 °C and 500 °C cause little changes in the size and number of the voids. Therefore, the formation of voids in the quenched-and-tempered samples is directly related to the graphites of the initial graphitized sample. The average size of graphites and voids is inversely proportional to the logarithm of their number density. When the as-rolled sample is completely graphitized, its ultimate tensile strength decreases from 928 to 494 MPa and its tensile elongation increases from 20.7 to 34.0%, indicating that the medium-carbon high-Si steel is substantially softened through graphitization treatment. Moreover, subsequent quenching and tempering treatment at 500 °C increases its ultimate tensile strength to 1168 MPa. The drastic softening through graphitization and significant strengthening through subsequent quenching and tempering exhibit the possibility of the application of medium-carbon, high-Si steels as cold heading quality steels for manufacturing fastener components.

Keywords High-silicon steel · Microstructure · Graphite · Void · Mechanical properties

1 Introduction

Good ductility and low strength are essential for initial materials of cold-formed steel components. For instance, high-strength bolts are usually produced from hot-rolled wires by following processes: spheroidizing, cold heading, thread rolling, and quenching and tempering to required strengths [1]. Spheroidizing heat treatment leads to the formation of the microstructure consisting of spherical carbide particles uniformly dispersed in a ferrite matrix. Such a microstructure results in high ductility because continuous ductile ferrite matrix and coarse, separated carbide particles provide

little resistance to dislocation motion during plastic deformation. Cold heading quality (CHQ) steels used for the production of fasteners such as bolts, screws, nuts, rivets, and nails are generally low-carbon steels with approximately 0.08%–0.3% carbon contents in order to secure high cold-forgeability [2–5]. In these low-carbon steels, although the strength of cold-formed steels can be increased through quenching and tempering heat treatment, the strength improvement is limited due to the low carbon content. Accordingly, medium-carbon steels > 0.3% C is necessary to manufacture fastener components with enhanced strength. In addition, to effectively soften the medium-carbon steels and secure good cold-forgeability, an appropriate heat treatment method other than spheroidizing heat treatment is required.

Spheroidized microstructures are known to be the most stable microstructure found in plain carbon steels [1]. However, spheroidizing heat treatment requires long treatment times (~12–20 h) for the diffusion-dependent nucleation and growth of spherical particles [6–8]. Thermodynamically,

✉ Sung Hyuk Park
sh.park@knu.ac.kr

¹ School of Materials Science and Engineering, Kyungpook National University, Daegu 41566, Republic of Korea

² POSCO Technical Research Laboratories, POSCO, Pohang 37859, Republic of Korea

although the most stable state of carbon is graphite, carbon generally exists as a metastable phase (cementite, Fe_3C) in conventional steels. However, in high-Si steels, graphite can be formed instead of cementite during heat treatment because Si is a strong ferrite-stabilizing element and its addition causes the destabilization of cementite [9–11]. In addition, the addition of alloying elements such as Al, Ti, and B leads to the formation of nitride or carbide particles, such as AlN , TiC , TiN , and BN , which promotes graphitization by acting as graphite nucleation sites [12–14]. It has recently reported that a $\text{Fe-0.38C-1.82Si-1.44Al}$ steel with a ferrite + pearlite structure is completely graphitized through short heat treatment within 4 h at $680\text{ }^\circ\text{C}$ [14]. Moreover, our previous study demonstrated that complete graphitization occurs within only 2 h at $700\text{ }^\circ\text{C}$ in a medium-carbon high-Si steel (Fe-0.55C-2.3Si) with a small grain size of $40\text{ }\mu\text{m}$ [15]. In medium-carbon steels containing high Si contents of $\sim 2\text{ wt}\%$, a greater softening effect can be achieved in a shorter time through graphitization heat treatment as compared to that of the spheroidizing heat treatment in conventional steels [16]. Because of these advantages of graphitization heat treatment, many studies have been conducted on the effects of alloying elements, pre-deformation, grain size, and initial microstructure on the graphitization behavior of high-Si steels [9, 17–19]. When medium-carbon high-Si steels are used as CHQ steels for manufacturing fastener components, the graphitized steels are subjected to quenching and tempering heat treatment after cold forging. However, previous researchers have predominantly aimed at addressing the graphitization rate during heat treatment, and no study has been conducted on the changes in the microstructure and mechanical properties of graphitized steels by successive heat treatments. Therefore, we aim to investigate the variations in graphite and tensile properties of graphitized medium-carbon high-Si carbon steels during austenitizing and tempering heat treatments, which belong to the quenching and tempering process. Moreover, the effects of the initial graphite size on the microstructural variation are also analyzed by heat-treating three graphitized samples with different graphite sizes.

2 Experimental procedure

A hot-rolled medium-carbon high-Si steel, Fe-0.55C-2.3Si (wt%), containing $\sim 30\text{ ppm}$ of N, was used in this study. The microstructure of steels greatly varies with a change of processing parameters such as temperature and cooling rate [20–23]. To control the graphite size, the as-rolled steel was heat-treated at different temperatures with a range of $700\text{--}750\text{ }^\circ\text{C}$ for 4 h. Consequently, three fully graphitized samples with different average graphite sizes were obtained; they hereafter denoted as G1, G2, and G3 samples,

respectively. The fully graphitized samples were heat-treated at $900\text{ }^\circ\text{C}$ for 4 h to dissolve graphite into the matrix and then were water-quenched; these heat-treated samples hereafter denoted as as-quenched samples. To analyze the variations in microstructure and mechanical properties with subsequent tempering treatment, the as-quenched samples were heat-treated at $300\text{ }^\circ\text{C}$ and $500\text{ }^\circ\text{C}$ for 1.5 h; these quenched-and-tempered samples hereafter denoted as QT300 and QT500 samples, respectively.

The microstructures of the as-rolled, graphitized, as-quenched, and quenched-and-tempered samples were observed using optical microscopy (OM) and scanning electron microscopy (SEM). For microscopic observations, the samples were progressively ground with finer grades of silicon carbide paper (from #120 to #2000) and then mechanically polished with $3\text{ }\mu\text{m}$ and $1\text{ }\mu\text{m}$ diamond pastes. After polishing, the as-rolled sample was etched using 2% Nital solution to observe the grain boundaries and pearlite structure. In contrast, the other samples were not etched to focus on the observation of graphites and voids. The size and number of graphites in the graphitized samples and voids in the as-quenched and quenched-and-tempered samples were measured using OM images by means of the threshold algorithm of the ImageJ program. These measurements of the size and number of graphites and voids were performed in a 3.3 mm^2 area. For tensile tests, dogbone-shaped rod specimens with gauge dimensions of 25 mm length and 6 mm diameter were machined from the as-rolled, graphitized, and QT500 samples in accordance with ASTM Standard E8 [24]; the loading axes of these specimens were parallel to the rolling direction. The tensile tests were performed at room temperature using the Instron 5985 universal hydraulic testing machine at a strain rate of $1 \times 10^{-3}\text{ s}^{-1}$.

3 Results and discussion

Figure 1a, b shows the optical and SEM micrographs of the as-rolled sample, respectively. The as-rolled Fe-0.55C-2.3Si steel has an average grain size of $38\text{ }\mu\text{m}$ and consists of proeutectoid ferrite and pearlite, which is the typical microstructure of hypoeutectoid steels (i.e., steels having carbon content less than the eutectoid solid solution). The proeutectoid ferrite exhibits a continuous network surrounding the pearlite colonies because ferrite is usually formed at the prior austenite grain boundaries during cooling from the austenite phase field (Fig. 1a). The pearlite colonies have a lamellar structure of alternating layers of ferrite and cementite, and the pearlite interlamellar spacing is $\sim 300\text{ nm}$ (Fig. 1b).

Figure 2 shows the microstructural evolution of the as-rolled sample during graphitization heat treat at $700\text{ }^\circ\text{C}$. When Fe-0.55C-2.3Si is heat-treated at temperatures

Fig. 1 **a** Optical and **b** SEM micrographs of the as-rolled Fe–0.55C–2.3Si. d_{avg} denotes the average grain size

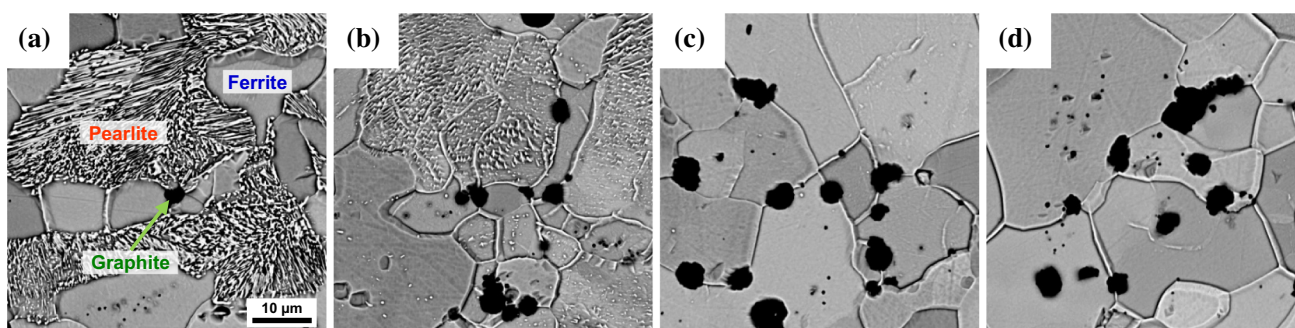
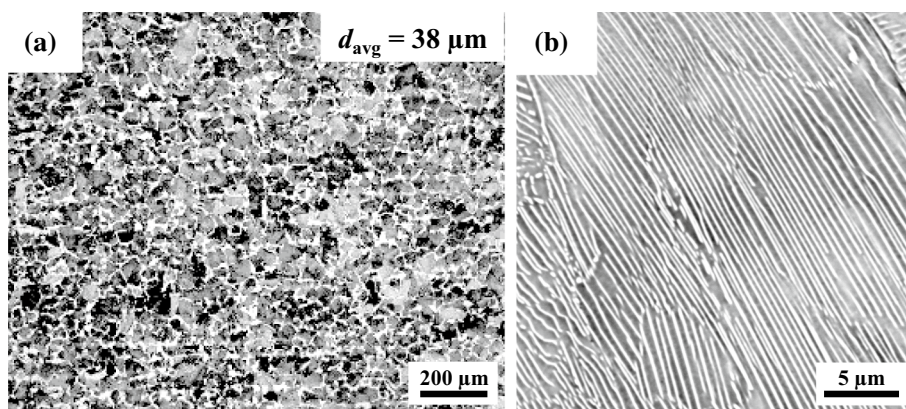


Fig. 2 SEM micrographs of Fe–0.55C–2.3Si graphitized at 700 °C for **a** 0.5, **b** 1, **c** 2, and **d** 4 h

slightly lower than Ac1 temperature (~ 764 °C for the tested steel), metastable cementite phase decomposes into Fe and C, and graphite is formed through the diffusion and aggregation of decomposed carbon [9, 12]. In addition, since graphite consists of only carbon atoms, Fe atoms existed in a position where the graphite is formed move out to the surroundings [25, 26]. As shown in Fig. 2, with an increase in the heat treatment time, the cementite phase gradually disappears, and more graphites are formed. Most of the formed graphites are nucleated at the ferrite-pearlite grain boundaries (i.e., the interface between proeutectoid ferrite and pearlite) because of a high diffusion rate of carbon atoms at these boundaries by their high energy and disordered atomic arrangements [15]. In the sample heat-treated for 1 h, it can be seen that the cementite phase is preferentially decomposed around graphites (Fig. 2b). As the heat treatment time increases from 0.5 to 2 h, both the number and size of graphites increase; the sample heat-treated for 2 h exhibits a ferrite + graphite structure without any residual pearlite (Fig. 2c). After the graphitization is completed, the nucleation and growth of graphites do not occur during further heat treatment; thus, the graphitized structure remains unchanged (Fig. 2d).

Optical micrographs of the fully graphitized samples are shown in Fig. 3. All the samples have a microstructure

consisting of ferrite and graphite, which is homogeneously distributed in the ferrite matrix. Since the diffusivity of carbon increases with increasing temperature, reducing the temperature of graphitization treatment decreases the size of graphites [27, 28]. Therefore, the G3 sample graphitized at the highest temperature has the largest graphite size. The average graphite sizes of the G1, G2, and G3 samples are 3.0, 6.1, and 10.4 μm , respectively (Fig. 3). In steel, the total volume fraction of graphites that can be formed by heat treatment is determined by the carbon content of steel and is independent of graphitization treatment conditions including graphitization temperature [29]. Therefore, as the average graphite size increases in steel, their number density decreases. In this study, the G1 sample with the smallest graphite size has the highest number density of graphites (1404 mm^{-2}), whereas the G3 sample with the largest graphite size has the lowest number density of graphites (191 mm^{-2}).

When the graphitized samples are subjected to austenitizing heat treatment, graphites are decomposed into carbon atoms, which are then dissolved into the matrix. SEM micrographs in Fig. 4 show the decomposition process of graphite in the G3 sample during austenitizing heat treatment at 900 °C. As shown in Fig. 4, the size of graphite gradually decreases with increasing austenitizing time, and

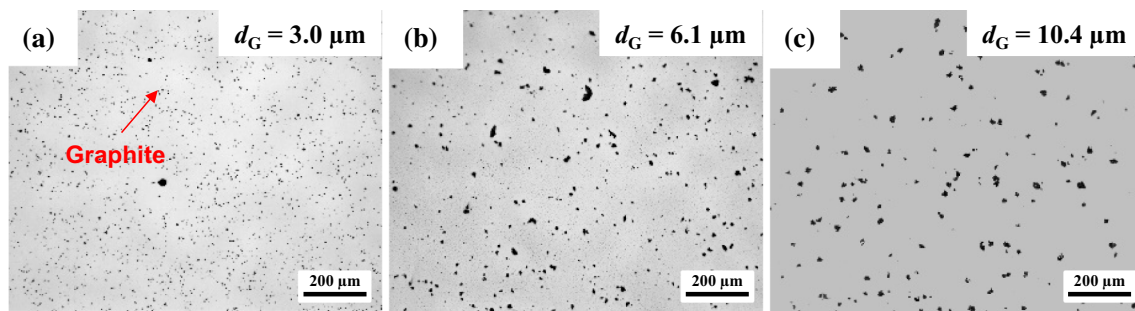


Fig. 3 Optical micrographs of the fully graphitized samples: **a** G1, **b** G2, and **c** G3. d_G denotes the average graphite size

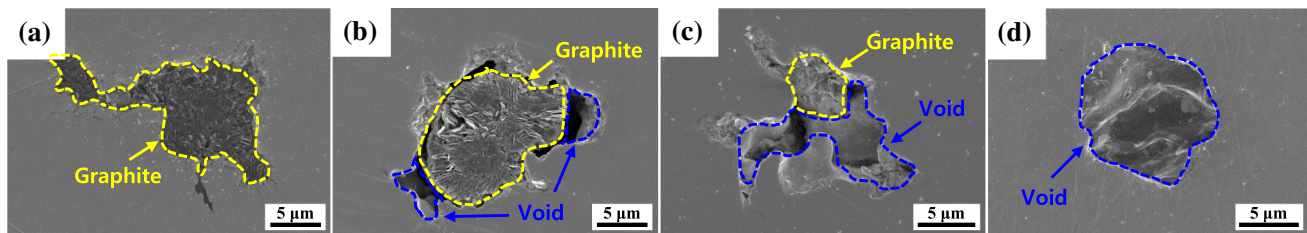


Fig. 4 SEM micrographs showing void formation at the graphite site during austenitizing treatment: **a** fully graphitized G3 sample and **b–d** subsequently austenitized samples at 900 °C for **b** 5, **c** 10, and **d** 120 min

graphite is completely dissolved after austenitizing for 2 h. Since ferrite has a very small carbon solubility of 0.022 wt% and graphite consists of only carbon, the decomposition of graphite begins at the interface between ferrite and graphite due to the substantially large difference in carbon concentration. Moreover, voids remain at positions where graphite is decomposed (Fig. 4b). As the decomposition of graphite continues, the size of the residual graphite decreases, and the size of the voids increase (Fig. 4c). After austenitizing treatment for 2 h, graphite is completely decomposed and dissolved, and the preexisting graphite locations remain void. Consequently, the void size is almost the same as that of the initial graphite (Fig. 4d), indicating that at heat treatment temperatures above A_{c3} , graphite dissolution in graphitized steels forms voids during austenitizing treatment because the diffusion coefficient of Fe at 900 °C ($2.42 \times 10^{-8} \text{ m}^2/\text{s}$ [30]) is significantly lower than that of carbon ($1.05 \times 10^{-7} \text{ m}^2/\text{s}$ [31]).

The optical micrographs of the G1, G2, and G3 samples heat-treated at 900 °C for 2 h and then water-quenched are shown in Fig. 5. Since the equilibrium phase at 900 °C belongs to the austenite single-phase region in the Fe–2Si–C equilibrium phase diagram, the graphites in the graphitized samples are completely dissolved into the matrix. All the as-quenched samples contain numerous voids at the positions of the dissolved graphites. Similar to the average graphite size of the graphitized samples, the average void size of the as-quenched samples is in the order of $G1 < G2 < G3$

(Fig. 5a–c). In contrast, the number density of voids of the as-quenched samples is in the order of $G1 > G2 > G3$, which is consistent with the order of the number density of graphites of the graphitized samples. In addition, the voids have an irregular shape, resulting from the morphology of graphites before heat treatment (Fig. 5d–f). Figure 6a, b shows the average size and number density of the graphites in the graphitized samples and the voids in the as-quenched samples, respectively. At a given graphitized sample, the average size of voids tends to be slightly larger than that of graphites before heat treatment, and the number density of voids is somewhat lower than that of graphites. However, the average size and number density of voids in each as-quenched sample match well with those of graphites in the corresponding graphitized sample. These results indicate that the size, number, and morphology of voids formed during austenitizing heat treatment are directly related to the graphites of the graphitized samples.

To analyze the variations in the size and number of voids during subsequent tempering, the as-quenched G1, G2, and G3 samples were heat-treated at 300 °C and 500 °C. At both tempering temperatures, the average void size of the QT samples is in the order of $G1 < G2 < G3$, and the void number per unit area is in the order of $G1 > G2 > G3$; these aspects are consistent with those of the as-quenched samples (Fig. 7). The average size and number density of voids of the as-quenched and QT samples are shown in Fig. 8a, b, respectively. At a given

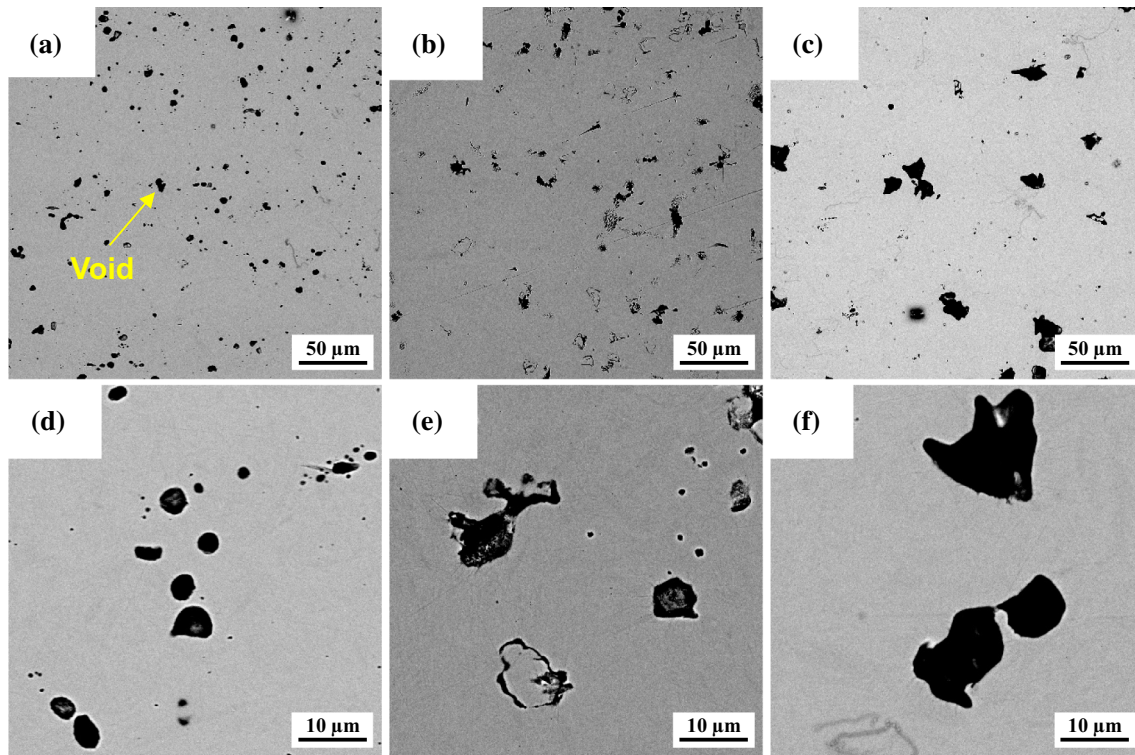


Fig. 5 Optical micrographs at **a–c** low and **d–f** high magnifications of as-quenched **a, d** G1, **b, e** G2, and **c, f** G3 samples

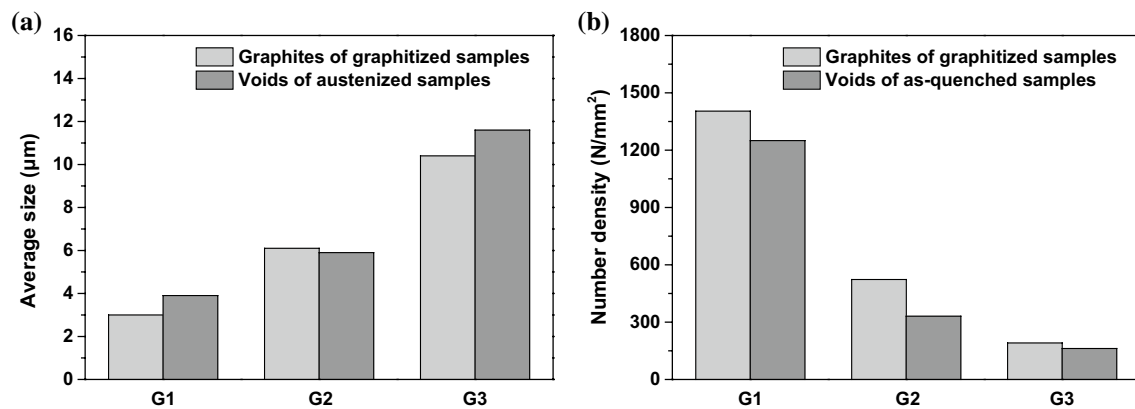


Fig. 6 Comparison bar charts of **a** average sizes and **b** number densities of graphites in the graphitized samples and voids in the as-quenched samples

graphitized sample (G1, G2, or G3), the average void sizes of the as-quenched, QT300, and QT500 samples are similar, and their void number is also almost the same. These results mean that the subsequently conducted tempering treatment does not affect the size and number of the pre-existing voids. From the fact that the size and number of voids in the as-quenched sample are strongly dependent on those of graphites of the graphitized sample, it can be concluded that the formation of voids in the QT samples

is responsible for the graphites of the initial graphitized samples.

Figure 9a, b shows the relationships between average size and number density for the graphites in the graphitized samples and the voids in the as-quenched and QT samples, respectively. As mentioned earlier, although the size and number of graphites depend on the graphitization heat-treatment conditions, the total volume fraction of graphites that can be formed in steel depends on the

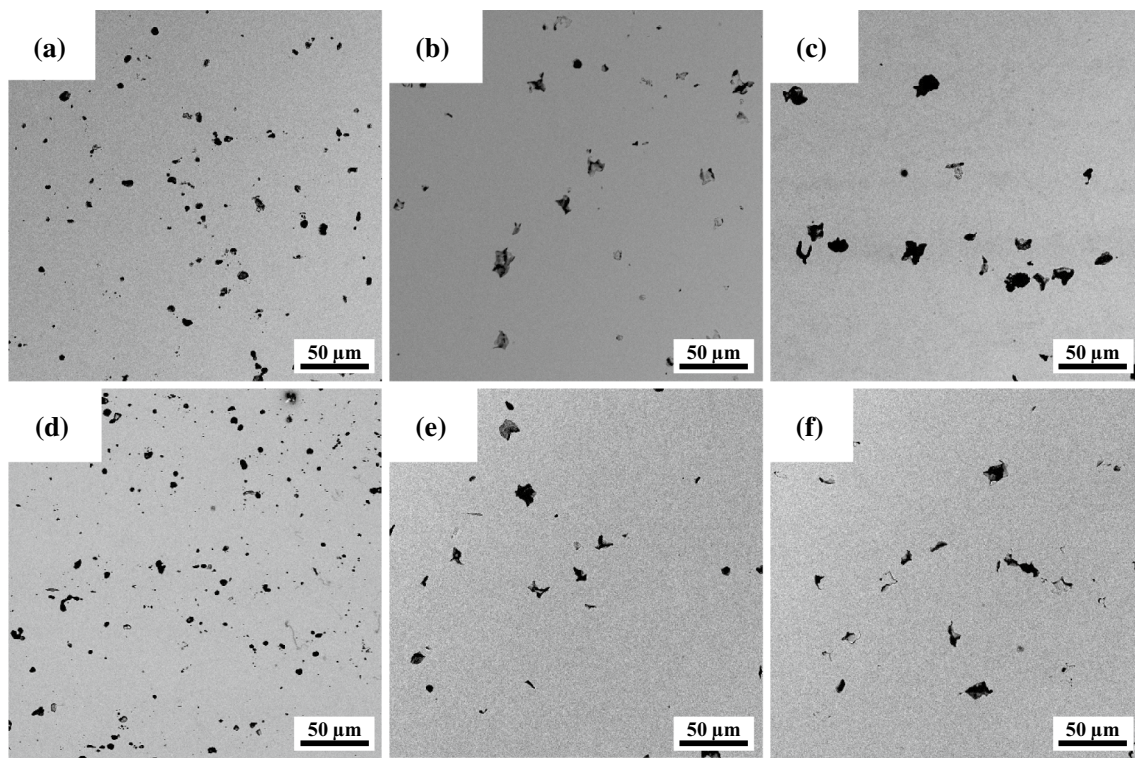


Fig. 7 Optical micrographs of the **a, d** G1, **b, e** G2, and **c, f** G3 samples quenched and tempered at **a–c** 300 °C and **d–f** 500 °C

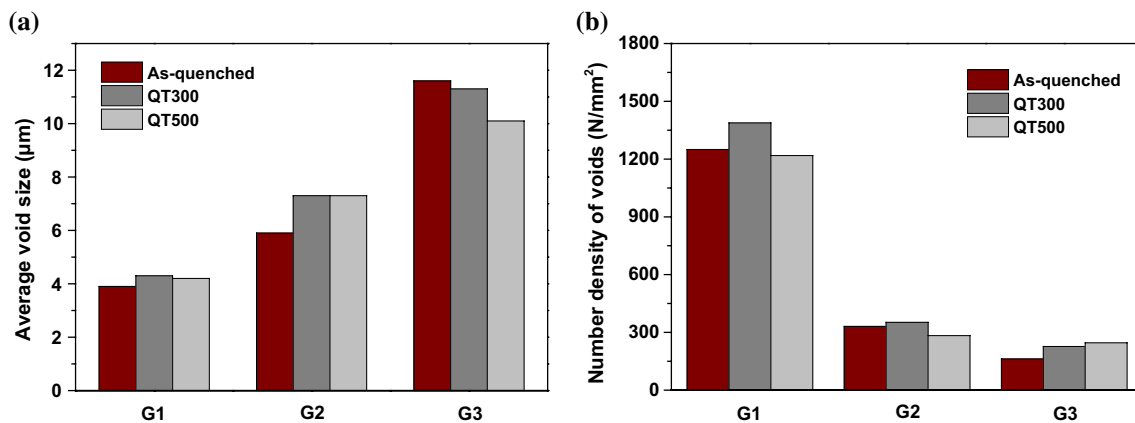


Fig. 8 Comparison bar charts of **a** average sizes and **b** number densities of voids in the as-quenched samples and the quenched and tempered (QT) samples

carbon content. Accordingly, smaller-sized graphites exist at a higher number density in the same steel. In addition, the voids in the as-quenched and QT samples are formed due to graphites before heat treatment, so their average sizes and number densities share the same inverse relationship as that of graphites. As shown in Fig. 9, the average size (d) was inversely proportional to the logarithm of their number density (ρ) for graphites and voids. The best-fitting relationship for graphites is $d = 29.7 - 8.6 \cdot \log(\rho)$

(Fig. 9a), which is almost the same as that for voids, $d = 27.4 - 7.6 \cdot \log(\rho)$ (Fig. 9b).

The tensile stress–strain curves of the as-rolled, graphitized, and QT500 samples are shown in Fig. 10. Although the G1, G2, and G3 samples have different sizes and numbers of graphites, their tensile strength and elongation are nearly the same, which means that the graphites in the graphitized samples have a negligible effect on the tensile properties of the samples. In addition, the tensile properties

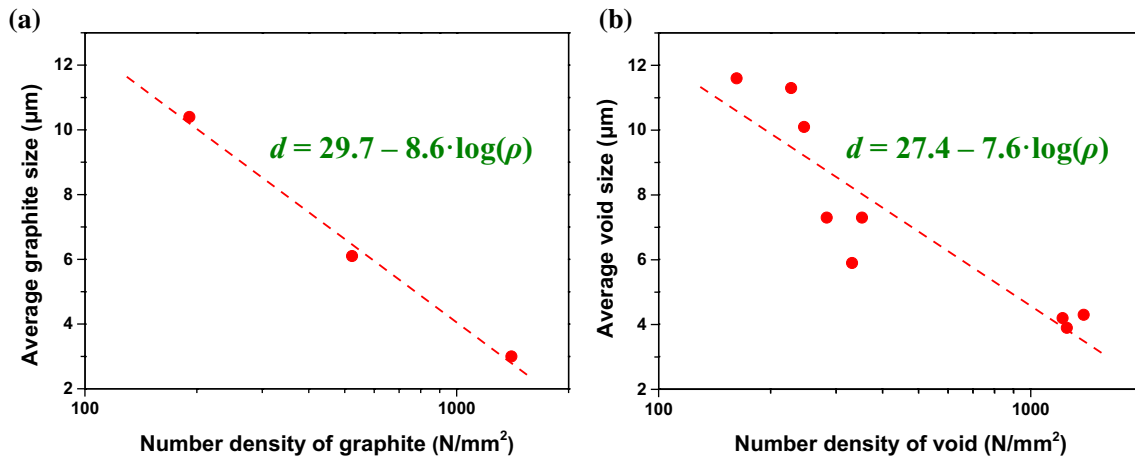


Fig. 9 Average size versus number density of **a** graphites in the graphitized samples and **b** voids in the as-quenched and quenched-and-tempered samples

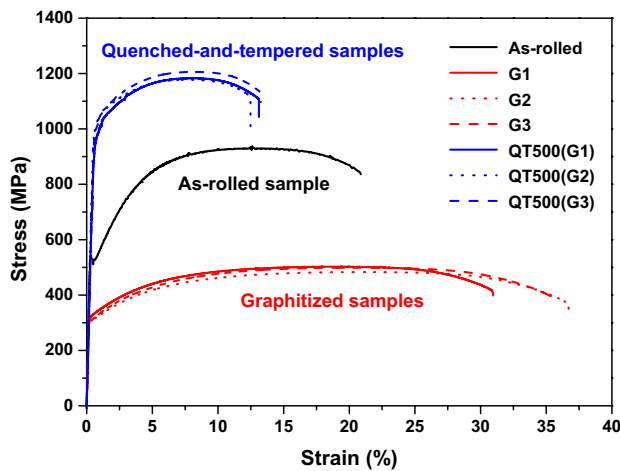
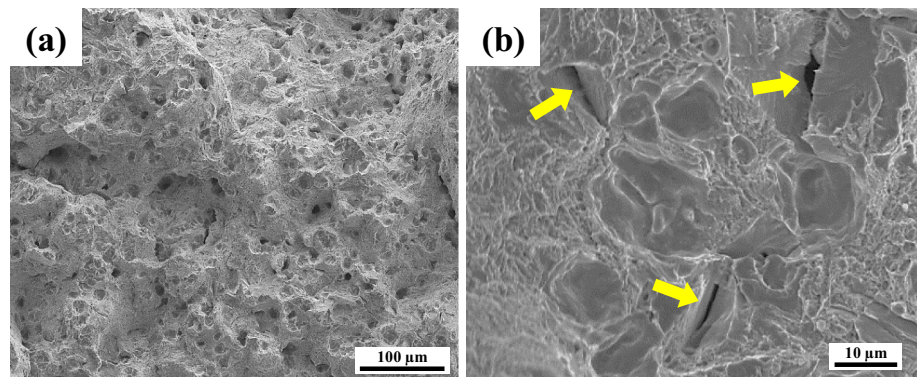


Fig. 10 Engineering tensile stress–strain curves of the as-rolled, graphitized, and quenched and tempered at 500 °C (QT500) samples

of the G1, G2, and G3 samples quenched-and-tempered at 500 °C (i.e., QT500 samples) are virtually the same. As the sizes of 3-dimensional lattice defects such as voids and

particles increase, the tensile elongation of metallic materials generally decreases due to the enhanced stress concentration at the defects and resultant premature fracture [32–34]. Figure 11 shows the fracture surfaces of the tensile tested specimen of the QT500(G3) sample, that is, the G3 sample quenched-and-tempered at 500 °C. The fractured specimen exhibits a ductile fracture mode with numerous dimples (Fig. 11a), and some sharp micro-cracks can be observed in the high-magnification fractograph (see the yellow arrows in Fig. 11b). These cracks are likely formed by voids existed in the sample because both the cracks and voids have a similar size ($\sim 10 \mu\text{m}$). However, the size of the cracks generated in some voids is similar to that of the dimples, and these cracks rarely propagate (Fig. 11b). These results suggest that the voids with sizes of 4.2–10.1 μm in the QT500 samples do not affect the tensile ductility of the samples. Therefore, three QT500 samples, which are obtained by QT treatment for the G1, G2, and G3 samples, have similar tensile elongations despite the considerable differences in the size and number of voids. Such ineffectiveness of the voids of the QT500 samples on their tensile ductility is also evidenced by the comparison of tensile properties with other QT steels

Fig. 11 SEM fractographs at **a** low and **b** high magnifications of the fractured tensile specimen of QT500(G3) sample. Yellow arrows in **b** indicate the void-initiated cracks



with no voids. Figure 12 shows the ultimate tensile strength (UTS) and tensile elongation of various QT steels with different alloy compositions and QT treatment conditions [35–41]. It can be seen that the UTS is inversely proportional to the elongation, which is a typical trade-off between strength and ductility in metals. As shown in Fig. 12, the tensile properties of the QT500 samples lie within the inverse relationship range of the other QT steels. This compared elongation of the QT500 samples to the other QT steels with similar strength indicates that the voids in the QT500 samples do not cause the degradation of tensile properties of the samples.

The tensile yield strength (TYS), UTS, and total elongation (EL) of the as-rolled sample and the average values of TYS, UTS, and EL for the graphitized samples and QT500 samples are shown in Fig. 13a. The graphitization

heat treatment leads to drastic decreases in both TYS (from 521 to 312 MPa) and UTS (from 928 to 494 MPa) because the relatively hard pearlite of the as-rolled sample changes to soft ferrite and graphites. It is known that the graphitization of cementite results in a considerable increase in the ductility and workability of steels [29, 42, 43]. In this study, the average EL of the graphitized samples (34.0%) is much larger than that of the as-rolled sample (20.7%). The reduced strength and improved ductility by graphitization show that graphitization heat treatment is a very effective method to soften the medium-carbon high-Si steel with a ferrite + pearlite structure. Through the application of subsequent QT heat treatment, the TYS and UTS of the graphitized samples substantially increase from 312 to 940 MPa and from 494 to 1168 MPa, respectively. Notably, the TYS and UTS of the QT500 samples are higher than those of the as-rolled sample; in particular, the TYS of the former (940 MPa) is 80% higher than that of the latter (521 MPa). This means that the strength of graphitized steels with high ductility can be greatly improved by QT heat treatment after cold metal forming. In contrast, the average EL of the graphitized samples largely decreases from 34.0% to 12.6% after QT heat treatment at the expense of an increase in strength.

The logarithm stress–strain curves in the plastic regime of the as-rolled, graphitized, and QT500 samples are presented in Fig. 13b. The strain hardening exponent n can be calculated from the slope of $\log(\text{true stress})$ – $\log(\text{true strain})$ curves based on the equation $\sigma = K\varepsilon^n$ (σ , K , ε , and n are the true stress, strength coefficient, true strain, and strain hardening exponent, respectively). A larger slope indicates a higher strain hardenability of the material. As shown in Fig. 13b, the slope of the logarithmic stress–strain curves is in the order of as-rolled sample > graphitized samples > QT500 samples. The average n values of the as-rolled,

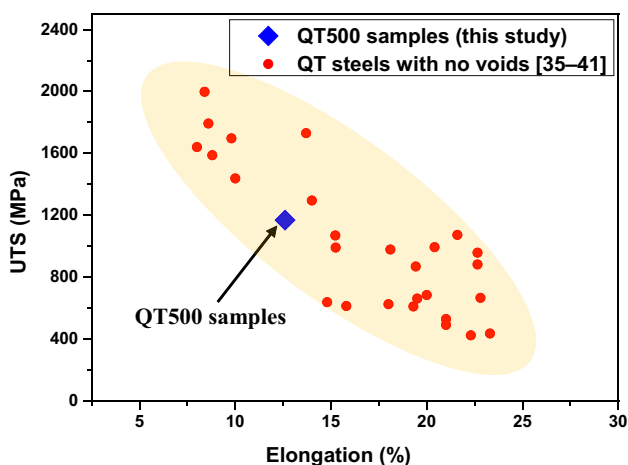


Fig. 12 Relationship between tensile strength and elongation of various QT steels

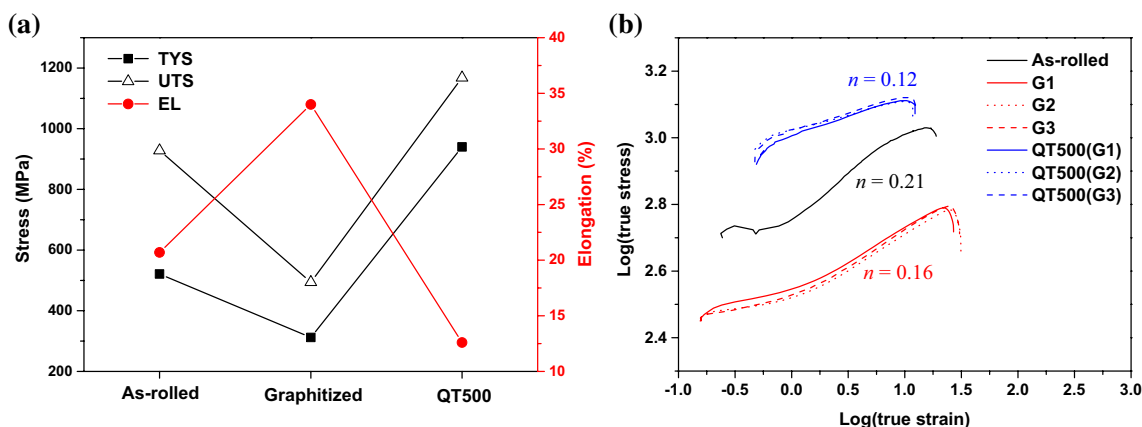


Fig. 13 a Effects of graphitization and subsequent QT treatments on the tensile properties of steel and b logarithmic stress–strain curves of the as-rolled, graphitized, and QT500 samples. TYS, UTS, EL, and n

denote the tensile yield strength, ultimate tensile strength, elongation, and strain hardening exponent, respectively

graphitized, and QT500 samples are 0.21, 0.16, and 0.12, respectively. The high strain hardening rate of the as-rolled sample is mainly attributed to the presence of the pearlite phase. A pearlite colony consists of alternating layers of soft ferrite and hard cementite, and this two-phased lamellar structure leads to the formation of many geometrically necessary dislocations during plastic deformation owing to the nonuniform deformation at the ferrite-pearlite interface [44]. Therefore, the as-rolled sample exhibit a high strain hardening behavior during tensile deformation. The graphitized samples with a ferrite + graphite structure show a lower strain hardening rate than the as-rolled sample with a ferrite + pearlite structure because graphite has very low strength and hardly causes stress concentration during deformation. The QT500 samples with a tempered martensite structure have the lowest strain hardening rate; their average n value is smaller even than that of the graphitized samples comprising soft ferrite and graphites. Tempering treatment leads to a decrease in the lattice distortion and dislocation density of martensitic steels. However, the QT500 samples undergone water-quenching at a high austenitizing temperature (900 °C) have much more abundant dislocations than the graphitized samples undergone air-cooling at relatively lower temperatures (700–750 °C). Therefore, the QT500 samples have high YS due to their high initial dislocation density but exhibit low strain hardening behavior because not only the dislocation generation but also the dislocation annihilation occurs during tensile deformation through dynamic recovery.

The results of this study demonstrate that high cold forgeability can be achieved even in medium-carbon steel with a carbon content of 0.55% through softening via graphitization heat treatment. In addition, the time taken for completion of graphitization is much shorter than that required in conventional spheroidizing heat treatment [15], leading to energy saving and efficiency enhancement in manufacturing processing. Moreover, as graphites are completely dissolved in the matrix by austenitizing treatment, all of the carbon content added in the steel can be exploited to improve the strength of the steel through subsequent QT treatment. Consequently, cold-formed high-strength steel products can be fabricated using medium-carbon or high-carbon high-Si steels through a sequential process: graphitization, cold forming, and quenching and tempering.

4 Conclusions

The variations in the microstructure and mechanical properties of the Fe–0.55C–2.3Si steel during graphitization heat treatment and subsequent quenching and tempering heat treatment have been investigated. The microstructure consisting of proeutectoid ferrite and pearlite of the as-rolled

sample changes to a more ductile microstructure with uniformly dispersed fine graphites in the ferrite matrix after graphitization treatment. These graphites are completely dissolved in the ferrite matrix after austenitizing treatment at 900 °C, and preexisting graphite positions remain as voids. The size, number, and morphology of voids formed in the as-quenched samples are nearly the same as those of graphites in the graphitized samples. Accordingly, the presence of graphites with a larger size leads to the formation of larger voids. The subsequently conducted tempering treatment does not affect the size and number of the preexisting voids. Consequently, the formation of voids in the quenched-and-tempered samples is directly related to the presence of graphites of the initial graphitized sample. For both graphites and voids, the average size is inversely proportional to the logarithm of the number density. When the as-rolled sample is subjected to graphitization treatment, the UTS of the sample decreases from 928 to 494 MPa and its EL increases from 20.7% to 34.0%, indicating the occurrence of significant softening of the steel by graphitization. After subsequent quenching and tempering treatment at 500 °C, the UTS of the sample substantially increases to 1168 MPa, but its elongation decreases to 12.6% at the expense of strength increase. The differences in the size and number of graphites or voids have a negligible effect on the tensile properties of the samples.

Acknowledgements This work was supported by grants from Pohang Iron and Steel Company (POSCO) (No. 2018Z022) and National Research Foundation of Korea (NRF) funded by the Korean government (MSIP, South Korea) (No. 2019R1A2C1085272).

References

1. G. Krauss, *Steels: Processing, Structure, and Performance*, 3rd edn. (ASM International, Cleveland, 2005)
2. L.I. Zhuang, W.U. Di, L. Wei, J. Iron Steel Res. Int. **19**, 64 (2012)
3. P.F. Thomason, Proc. Inst. Mech. Eng. **184**, 875 (1969)
4. H. Kim, M. Kang, C.M. Bae, H.S. Kim, S. Lee, Metall. Mater. Trans. A Phys. Metall. Mater. Sci. **45**, 1294 (2014)
5. Z. Li, J. Iron Steel Res. Int. **16**, 43 (2009)
6. M.J. Harrigan, O.D. Sherby, Mater. Sci. Eng. **7**, 177 (1971)
7. K.G. Ata, S.A. Meisam, J. Iron Steel Res. Int. **17**, 45 (2010)
8. H.M. Seok, K.H. Tae, Int. J. Chem. Nucl. Metall. Mater. Eng. **8**, 115 (2014)
9. K.D. Woo, J. Korean Soc. Heat Treat. **17**, 117 (2004)
10. A.A. Zhukov, Met. Sci. Heat Treat. **26**, 849 (1984)
11. P. Rubin, R. Larker, E. Navara, M.L. Antti, Metallogr. Microstruct. Anal. **7**, 587 (2018)
12. K. Banerjee, T. Venugopalan, Mater. Sci. Technol. **24**, 1174 (2008)
13. T. Iwamoto, T. Hoshino, A. Matsuzaki, K. Amano, ISIJ Int. **42**, S77 (2002)
14. K. He, H.R. Daniels, A. Brown, R. Brydson, D.V. Edmonds, Acta Mater. **55**, 2919 (2007)
15. Y.J. Kim, S.W. Bae, N.S. Lim, S.H. Park, Mater. Sci. Eng. A (2020). <https://doi.org/10.1016/j.msea.2020.139392>

16. M. Okonogi, M. Hashimura, H. Kanisawa, S. Katayama, *Nippon Steel Tech. Rep.* **80**, 16 (1999)
17. A. Inam, R. Brydson, D.V. Edmonds, *Mater. Charact.* **106**, 86 (2015)
18. S.A. Rounaghi, A.R. Kiani-Rashid, *Phase Trans.* **84**, 981 (2011)
19. J.X. Gao, B.Q. Wei, D.D. Li, K. He, *Mater. Charact.* **118**, 1 (2016)
20. H.L. Kim, S.H. Bang, J.M. Choi, N.H. Tak, S.W. Lee, S.H. Park, *Met. Mater. Int.* (2019). <https://doi.org/10.1007/s12540-019-00500-2>
21. F. Najafkhani, H. Mirzadeh, M. Zamani, *Met. Mater. Int.* **25**, 1039 (2019)
22. M. Kalantar, H. Najafi, M.R. Afshar, *Met. Mater. Int.* **25**, 229 (2019)
23. S.K. Basantia, A. Bhattacharya, N. Khutia, D. Das, *Met. Mater. Int.* (2019). <https://doi.org/10.1007/s12540-019-00519-5>
24. W. Shyam, *ASTM E8/E8M-11 Standard Test Methods for Tension Testing of Metallic Materials* (ASTM, Philadelphia, 2011)
25. H. Sueyoshi, K. Suenaga, *Nippon Kinzoku Gakkai-si* **43**, 333 (1979)
26. H. Sueyoshi, K. Suenaga, R. Tanaka, *Nippon Kinzoku Gakkai-si* **49**, 20 (1985)
27. K. Oikawa, H. Mitsui, T. Ebata, T. Takiguchi, T. Shimizu, K. Ishikawa, T. Noda, M. Okabe, K. Ishida, *ISIJ Int.* **42**, 806 (2002)
28. A. Rosen, A. Taub, *Acta Metall.* **10**, 501 (1962)
29. Y. Yoshida, L. Cisar, S. Kamado, Y. Kojima, *Mater. Trans.* **44**, 468 (2003)
30. F.S. Buffington, K. Hirano, M. Cohen, *Acta Metall.* **9**, 434 (1961)
31. J. Ågren, *Acta Metall.* **30**, 841 (1982)
32. P. Haušild, C. Berdin, P. Bompard, N. Verdière, *Int. J. Press. Vessel. Pip.* **78**, 607 (2001)
33. X. Teng, H. Mae, Y. Bai, T. Wierzbicki, *Eng. Fract. Mech.* **76**, 983 (2009)
34. P.F. Liu, J.Y. Zheng, *J. Fail. Anal. Prev.* **10**, 212 (2010)
35. S.K. Dhua, A. Ray, D.S. Sarma, *Mater. Sci. Eng. A* **318**, 197 (2001)
36. Y. Kimura, T. Inoue, K. Tsuzaki, *J. Alloys Compd.* **577S**, S538 (2013)
37. A. Ohmori, S. Torizuka, K. Nagai, *ISIJ Int.* **44**, 1063 (2004)
38. W.S. Lee, T.T. Su, *J. Mater. Process. Technol.* **87**, 198 (1999)
39. A. Leiro, A. Roshan, K.G. Sundin, E. Vuorinen, B. Prakash, *Acta Metall. Sin. (Engl. Lett.)* **27**, 55 (2014)
40. M.S. Rashid, B.V.N. Rao, *Metall. Trans. A* **13**, 1679 (1982)
41. X. Xiong, F. Yang, X. Zou, J. Suo, *J. Nucl. Mater.* **430**, 114 (2012)
42. K.S. See, T.A. Dean, *J. Mater. Process. Technol.* **69**, 58 (1997)
43. L. Yuan, W. Shi, R. Shivpuri, F. Xu, D. Shan, *J. Mater. Process. Technol.* **243**, 456 (2017)
44. B. Karlsson, G. Linden, *Mater. Sci. Eng.* **17**, 209 (1975)

Publisher's Note Springer Nature remains neutral with regard to jurisdictional claims in published maps and institutional affiliations.